



Colocation and role of polyphosphates and alkaline phosphatase in apatite biomineralization of elasmobranch tesseræ[☆]



Sidney Omelon^{a,*}, John Georgiou^b, Fabio Variola^{c,d}, Mason N. Dean^e

^a Department of Chemical and Biological Engineering, University of Ottawa, Ottawa, Canada

^b Lunenfeld-Tanenbaum Research Institute, Mt Sinai Hospital, Toronto, Ontario, Canada

^c Department of Mechanical Engineering, University of Ottawa, Ottawa, Canada

^d Department of Physics, University of Ottawa, Ottawa, Canada

^e Department of Biomaterials, Max Planck Institute of Colloids and Interfaces, Potsdam-Golm, Germany

ARTICLE INFO

Article history:

Received 21 December 2013

Received in revised form 6 June 2014

Accepted 8 June 2014

Available online 16 June 2014

Keywords:

Elasmobranch
Mineralization
Tesseræ
Polyphosphate
Skeleton

ABSTRACT

Elasmobranchs (e.g. sharks and rays), like all fishes, grow continuously throughout life. Unlike other vertebrates, their skeletons are primarily cartilaginous, comprising a hyaline cartilage-like core, stiffened by a thin outer array of mineralized, abutting and interconnected tiles called tesseræ. Tesseræ bear active mineralization fronts at all margins and the tesseral layer is thin enough to section without decalcifying, making this a tractable but largely unexamined system for investigating controlled apatite mineralization, while also offering a potential analog for endochondral ossification. The chemical mechanism for tesseræ mineralization has not been described, but has been previously attributed to spherical precursors, and alkaline phosphatase (ALP) activity. Here, we use a variety of techniques to elucidate the involvement of phosphorus-containing precursors in the formation of tesseræ at their mineralization fronts. Using Raman spectroscopy, fluorescence microscopy and histological methods, we demonstrate that ALP activity is located with inorganic phosphate polymers (polyP) at the tessera–uncalcified cartilage interface, suggesting a potential mechanism for regulated mineralization: inorganic phosphate (Pi) can be cleaved from polyP by ALP, thus making Pi locally available for apatite biomineralization. The application of exogenous ALP to tissue cross-sections resulted in the disappearance of polyP and the appearance of Pi in uncalcified cartilage adjacent to mineralization fronts. We propose that elasmobranch skeletal cells control apatite biomineralization by biochemically controlling polyP and ALP production, placement and activity. Previous identification of polyP and ALP shown previously in mammalian calcifying cartilage supports the hypothesis that this mechanism may be a general regulating feature in the mineralization of vertebrate skeletons.

© 2014 Acta Materialia Inc. Published by Elsevier Ltd. This is an open access article under the CC BY-NC-ND license (<http://creativecommons.org/licenses/by-nc-nd/3.0/>).

1. Introduction

The mineralized skeletons of vertebrate animals – whether primarily cartilaginous or bony – share the same major extracellular components: water, collagenous and non-collagenous proteins and biological apatite [1,2]. Although vertebrate skeletons vary considerably in microstructure, a common necessity in their growth is the regulation of the location and timing of mineralization, so that tissues mineralize in controlled ways and mineralization is not a runaway process [3]. Mineralization of both bony [4] and cartilaginous [5] skeletons has been attributed to localized

activity of alkaline phosphatase (ALP), an enzyme that cleaves phosphoester bonds. However, the ALP substrate that provides inorganic phosphate (PO_4^{3-} : Pi) for apatite mineralization is still debated.

One potential ALP substrate is polyphosphate ($(\text{PO}_3^-)_n$: polyP). PolyP has been proposed as a Pi source for apatite biomineralization, as it exists as linear molecules of phosphate ions connected by phosphoester bonds, forms complexes with cations [6] and has been identified in calcifying cartilage and resorbing bone in bony skeletons [7]. Phosphate polymerization is a simple biological mechanism for accumulating and storing phosphate ions in a neutral pH environment without producing phosphate minerals [8]. When polymerized, Pi is not available for mineralization until it is cleaved from polyP, either spontaneously through hydrolytic degradation, or at an accelerated rate by a phosphatase enzyme (e.g. ALP). PolyPs could therefore be used as a flexible and precise

[☆] Part of the Biomineralization Special Issue, organized by Professor Hermann Ehrlich.

* Corresponding author. Tel.: +1 613 562 5800x6288.

E-mail address: somelon@uottawa.ca (S. Omelon).

means of transporting phosphate to mineralization sites without the danger of premature “off-site” mineralization. Demonstrating apatite mineralization chemistry in mammalian skeletons is problematic because sample preparation to obtain thin skeletal sections normally requires the use of water, which may affect unstable mineral precursors. The identification of putative, spherical, amorphous and unstable bone mineral precursors has previously only been achieved with either cryo-techniques [9,10] or anhydrous sample preparation techniques [11].

The skeletons of elasmobranch fishes (sharks, rays and relatives) offer a useful system for investigating the involvement of polyPs in biomineralization, in that mineralization fronts are abundant and readily accessible. Unlike nearly all other vertebrates, the skeletons of elasmobranchs are predominantly cartilaginous, composed largely of a soft, uncalcified cartilage (UC) core sheathed in a thin layer of mineralized blocks called tesserae [12,13] (Fig. 1). Each tessera is effectively a contained subunit, hundreds of microns wide and deep, sandwiched between the inner UC and outer fibrous perichondrium layers of the skeleton. Tesserae are filled with a rich network of tesseral cells housed in lacunar spaces in the mineralized tissue and connected by short “canalicular” passageways (Figs. 1 and 2) [12,14]. Tesserae cover the outer surface of most portions of the skeleton (e.g. a shark’s jaw would be coated by thousands of tesserae), are easily accessible, section without decalcifying and appear to grow on all surfaces throughout the animals’ lives [12]. Therefore, we expect every tessellated skeletal element to offer a huge array of apatite mineralization fronts (on every tesseral surface) available for analysis of growth and mineralization processes. Since elasmobranch skeletons, unlike bony ones, cannot remodel during growth [15,16], the tiling of the surface of the skeleton by discrete mineralized elements (tesserae) allows for a continued expansion of the rigid outer sheath while the inner cartilaginous core also grows in volume as the animals age [12]. Controlled, localized mineralization is therefore vital to the growth of this skeletal type, which is, from a morphological standpoint, particularly amenable to study.

Cartilage calcification at the mineralization front between UC and the underside of the tesserae (what we term the “chondral edge”; Fig. 2) was previously observed to involve small (<1 μm)

globular mineral structures, believed to accrete and grow the chondral surface of tesserae [13,17–19]. The globular mineral at the chondral edge of tesserae is reminiscent of “calcospheres” and other spherical vesicles that have been described in the literature as potential mineral precursors in bony skeletons [20–24], but without a specific definition of their composition. The “secretory” theory [25] (reviewed in Ref. [26]) posited that these calcospheres could act as mineral precursors, formed by cells and secreted into the extracellular matrix, for transformation into apatite in tissue at the mineralization front. In elasmobranch skeletons, this theory is supported by observations of a “cloud” of vesicular “blebs” at a distance from chondrocytes in pre-mineralizing cartilage [18,27]. Similar blebs have been observed in association with cartilage mineralization initiators in bony skeletons [28]. Recent literature identified amorphous, calcium and phosphorus-containing nano-scaled spheres in bone with cryo-sample preparation and analysis [9]. The Ca:P ratio of these spherical precursors was reported to be 0.75 ± 0.22 compared to 1.5 for bone mineral [9] and 1.67 for pure hydroxylapatite [29]. The low Ca:P ratio of these granules suggests that they may contain polyP, as the Ca:P ratio of a Ca-polyP complex is greater than 0.5 and less than 1.0 [11], depending on the polyP chain length.

PolyP depolymerization by water is thermodynamically driven [30], but the kinetics are slow. Once secreted by cells and transported to the extracellular mineralization site, polyP could be controllably broken down into Pi by the action of ALP; this local Pi concentration increase could form apatite [7]. Colocalization of ALP and polyPs in elasmobranch skeletons would provide strong support for our proposed regulation of mineralization by polyPs in tesserae. Although Eames et al. [5] previously identified ALP activity in pre-mineralizing embryonic elasmobranch skeletal elements, to our knowledge, no study has identified biochemical mechanisms of mineralized tissue formation and control in elasmobranch skeletons.

The goal of this study was to identify ALP and polyP at the chondral margin of tesserae at the optical microscopy scale of tissue analysis, using staining, fluorescence microscopy and Raman spectroscopy. To further test the hypothesis that polyP is an apatite precursor at this interface, exogenous ALP was applied to break down polyP and produce Pi in its place.

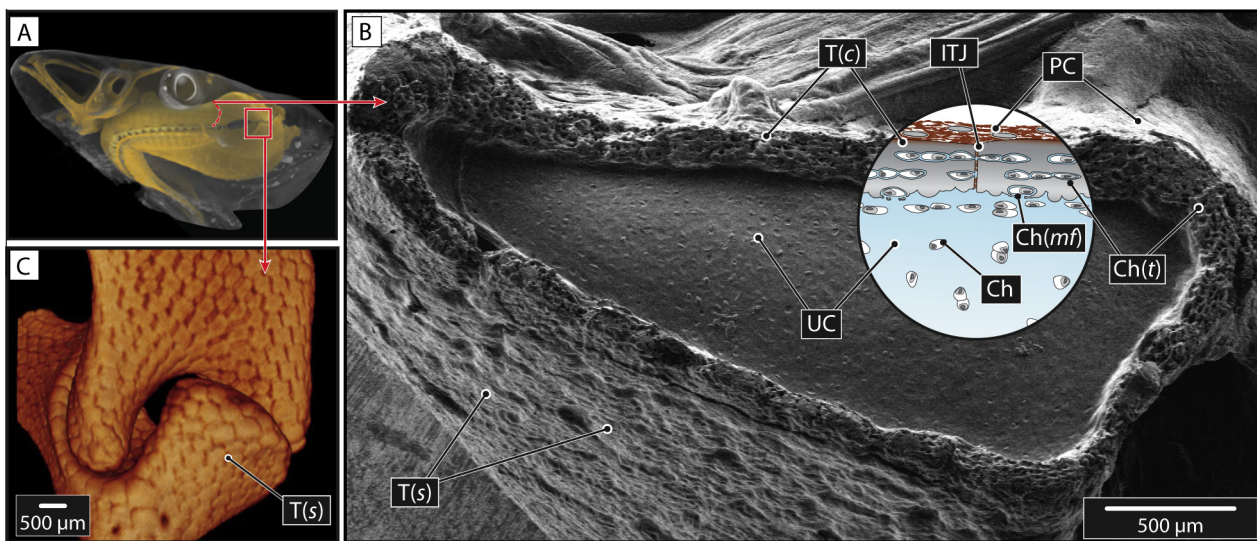


Fig. 1. Organization of tessellated cartilage in the skeletons of elasmobranch fishes. (A) CT scan of an example elasmobranch head skeleton (from a blue shark, *Prionace glauca*). (B) Cryo-scanning electron image of the cross-section of the tessellated upper jaw (from a stingray, *Urobatis halleri*). T(c): tesserae in cross-section; PC: perichondrium; UC: uncalcified cartilage; Ch: chondrocyte, Ch(mf): chondrocyte at the mineralization front becoming encapsulated in mineralized tissue; Ch(t): tesseral chondrocyte embedded in a lacunar space in tesserae; ITJ: fibrous intertesseral joint connecting adjacent tesserae; T(s): tesseral (perichondral) surface. (C) Magnification of the tessellated surface of a mandibular joint (from *U. jamaicensis*; anatomical location indicated by the red box in A). The anatomical schematic is a synthesis of available data from multiple works (e.g. Refs. [12,14,17,27,42,59]). Figure modified from Ref. [59] with permission from Elsevier.

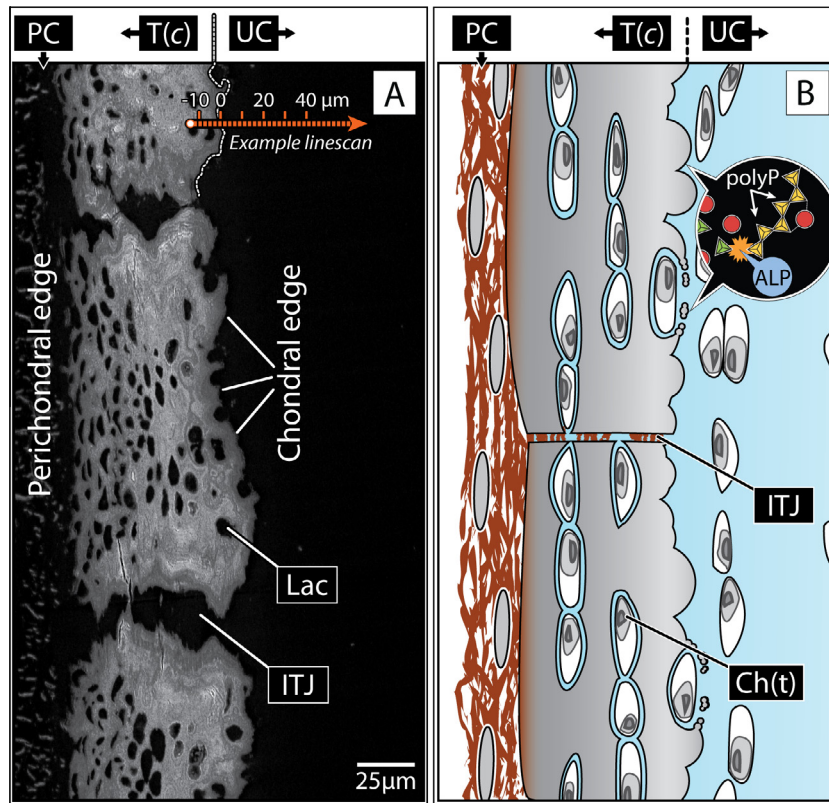


Fig. 2. Locations of hypothesized tesseral mineralization fronts shown (A) in a backscatter SEM image of a cross-section of a layer of tesseratae (T(c)) and (B) in a schematic of a similar region. Tesseratae are sandwiched between the outer perichondrium (PC) and the inner UC core of the skeleton and therefore have outer “perichondral” and inner “chondral” edges. We expected polyPs and ALP to localize at the latter edge, and so for most assays, we performed line scans extending from the tesseratae out into the UC (e.g. to quantify staining intensity; see Section 3 and the hypothetical line scan drawn in panel (A)). The tessera–UC border is set at 0 μm , with black arrowed boxes (top) indicating the location of tesseral material and UC relative to the tissue interface; these same arrowed boxes are used in most subsequent figures to clarify the location of the tessera–UC interface. Unmineralized features, like the fibrous intertesseral joints (ITJs) and the tesseral chondrocytes (Ch(t)) housed within lacunae (Lac), are not visible in the backscatter image but are depicted in the schematic. Adjacent lacunae are connected by short passageways, creating long “strings” of chondrocytes within tesseratae [14]. Compare with features in Fig. 1 for more anatomical context.

2. Theory

It is theorized that apatite biomineralization is controlled by the biochemical manipulation of phosphorus speciation by ALP. This section summarizes the concepts related to the theory that polyP is a molecule that concentrates P without producing a phosphate mineral, is a substrate for ALP and is a precursor for biological apatite.

Phosphorus is hypothesized to be concentrated by mitochondria in skeletal cells, and transported to extracellular mineralization sites as polyP, not as Pi [7]. PolyPs form strong complexes with calcium and other divalent ions [6], resulting in a calcium and phosphorus-rich complex that is non-crystalline. Amorphous calcium-polyP requires temperatures well beyond biological conditions to crystallize [31]. ALP cleaves the phosphoester bonds at the end of polyP, liberating many Pi molecules [32]. Because ALP has been identified in areas where tesseratae will form [5], we theorized that ALP may be collocated with polyP at the margins of the growing tesseratae. Here, ALP activity could control the local increase in Pi concentration by polyP depolymerization. Local increase in Pi concentration could exceed apatite saturation, and result in biologically controlled apatite formation within cartilaginous tissue [7].

In a previous study of mineralized spherules within calcifying cartilage, limited sample preparation (i.e. with as little processing as possible) was required to observe labile calcium and phosphorus species [33]. Therefore, to avoid degradation of labile mineral precursors (e.g. polyPs), the methodologies in this study focused largely around minimal sample preparation, involving cryo-cutting

and staining, with no embedding or further processing. As elasmobranch cartilage involves many interfaces of tissues with drastically different material properties (e.g. at the tesseral perichondral and chondral borders; Fig. 2), our cryo-sectioning techniques typically resulted in imperfect (non-planar) sections. However, this approach was vital to slow polyP removal and/or depolymerization.

We theorize that in previous studies of mineralized tissues, polyPs may not have been identified due to their inadvertent removal during sample preparation, as was noted in a study of polyP-containing acidocalcisomes in amoeba tissues [34]. The instability of a stained but unidentified component, which we interpret to have been polyP, exhibited a transient toluidine blue (TB) staining in the hypertrophic zone of fresh-cut and promptly stained calcifying cartilage [35]. Only when fresh samples were stained, were calcium and P-rich granules within and adjacent to mature and hypertrophic calcifying chondrocytes observed [33]. Others have identified Ca- and P-rich, electron-dense amorphous granules in mineralizing tissues only if the sample was prepared in anhydrous or cryo-conditions [9,22,36].

We tested the hypothesis that polyP is located in actively mineralizing sites by using different techniques for polyP identification within UC at the chondral surface of the tesseratae. The techniques used, in decreasing order of chemical specificity, were Raman spectroscopy [37,38], DAPI–polyP fluorescence [39,40] and TB metachromasia [41]. Pi, identified by von Kossa (VK) staining, is not expected to be present in the UC near the globular tessera mineralization front, as this tissue is not yet mineralized.

As ALP breaks down polyP, another strategy for polyP identification in calcifying cartilage is to demonstrate the disappearance of polyP with the application of exogenous ALP [7]. As Pi is released when polyP is broken down, it was also theorized that, following application of ALP, Pi should appear in the UC in regions where polyP had been observed in fresh sections. Therefore, in our elasmobranch model, ALP-treatment would be expected to decrease polyP (as evidenced by a decrease in DAPI or TB stain at the tessera–UC interface), with Pi identified in its place by VK staining (Fig. 2).

It should be noted that our methods do employ some simplifying assumptions. For example, we examine several species in this study (a function of sample availability), making the assumption that tesseral mineralization mechanisms are similar on a biochemical level across species and different skeletal elements. We consider this to be reasonable, given that all examined samples were from adult animals exhibiting tesserae of roughly similar size and shape, and given that our powder diffraction studies (see below) confirmed apatite as the mineral component in two species' tesserae, reinforcing previous observation from two other species [42,43] and suggesting commonality across elasmobranch taxa. Future investigations into potential variation between and within species (e.g. across ontogenetic stages) would be valuable.

The application of exogenous ALP was used to mimic and increase the rate of polyP depolymerization. Elasmobranch body temperatures are considerably lower than the temperatures used here to activate ALP (37 °C); however, as ALP has been found in pre-mineralization areas in young elasmobranch skeletons [5], we consider this a reasonable method for testing whether polyP in the cartilage could be depolymerized to Pi, although we recognize that the time scale of the activity would be considerably different in vivo. We also appreciate that other, unidentified, endogenous phosphatase enzymes may also degrade polyP to Pi. Finally, because some methods of detecting polyP in situ (i.e. within tissues) are not specific, we performed several techniques in combination to argue the presence of this transient species in mineralizing tissue, applying one non-specific optical histological technique [41], one specific fluorescence microscopy spectral technique (DAPI) [39,40] and Raman spectroscopy [37,38].

3. Materials and methods

3.1. Synchrotron powder diffraction

Skeletal samples of the stingrays *Dasyatis sabina* and *Myliobatis californica* were excised, freeze-dried and pulverized by hand. To compare elasmobranch tessera mineral with bone mineral, emu cortical bone powder was prepared for powder X-ray diffraction (XRD) as described previously [44]. Emu cortical bone was used as a proxy for human cortical bone, as the ratio of its dry composition (63 mineral: 31 organic matrix, with 1% fat [45]) is similar to the ratio of mineral to organic matrix (65:35) in human cortical bone [46], and as it has been used previously as a human cortical bone model [45,47].

Apatite biominerals were analyzed by the 11-BM mail-in service offered by the Argonne National Laboratories (University of Chicago, USA) [48]. The samples were scanned at ~30 keV, with a beam size of 1.5 mm × 0.5 mm, at room temperature. Estimates of crystallite sizes were made by fitting the peaks and measuring the full width at half maximum (FWHM) values for the (002) (long, c-axis), (310) and (222) (transverse axes) peaks with the CMPR program [49]. The instrument peak broadening was determined using published data for a standard material (LaB₆, NIST 660a) that was measured by the same beamline. The X-ray wavelength (0.413023 Å) and the K-value (0.9) were used in the Scherrer

equation to estimate the crystallite size, assuming negligible crystallite strain. Only one sample was analyzed for each of the three skeletal types, therefore no statistical tests were applied to these results.

3.2. Raman spectroscopy

The focus of this work was to identify Raman shifts in the UC at the subchondral tesseral margins (Fig. 2), as this is where polyP was hypothesized to be most concentrated and evenly distributed in order to act as a Pi source for mineral formation. Freeze-dried specimens of *Uroobatis halleri* jaws were reconstituted in 70% ethanol, cryo-microtomed and analyzed immediately by Raman spectrographic analysis. This immediate analysis was required because it was found that samples tended to collapse in thawing during slower sample preparation methods, resulting in drastic changes in the optical plane during data collection with the laser. The employed reconstitution method resulted in a strong and sustained polyP signal. In contrast, polyP signals in UC of fresh samples decreased rapidly; we attributed these fading polyP signals to the activation of endogenous phosphatase enzymes hydrolyzing polyP as the sample defrosted.

Cryo-microtomed 100 µm sections were mounted on quartz slides. Frozen sections were promptly imaged under light at 20× to identify and focus on the tessera–UC interface. Linear Raman scans were made along a ~100 µm hand-drawn line, perpendicular to the tessera–UC interface and extending from the middle of a tessera into the UC (see Fig. 2A). Spectra were acquired with a confocal Raman microscope (CRM200, WITec GmbH, Ulm, Germany) equipped with a P-500 piezo-scanner (Physik Instrumente, Karlsruhe, Germany) and a CCD (Princeton Instruments Inc., Trenton, NJ). A 785 nm laser (Toptica Photonics AG, Graefelfing, Germany) was used to generate Raman scattering while minimizing autofluorescence. 20 spectra were collected per line with 2 s integration times and a step size of ~5 µm.

WITec Project (v. 2.10, WITec GmbH, Ulm, Germany) software was used to investigate Raman shifts for Pi and polyP by using the sum filter. For each line scan, peak intensity (counts) vs. distance (µm) data were generated. The sum filter calculates peak intensities between selected relative shift wave numbers, generating a peak area value. Pi intensity was calculated between 930 and 980 cm⁻¹ [50], and the polyP intensity was calculated with the PO₂⁻ symmetrical stretching vibration between 1145 and 1175 cm⁻¹ ([51] cited in Ref. [37]). As Pi Raman scattering intensity was larger than that of polyP, each sum filter data set (Pi or polyP) was normalized with respect to its maximum value along the line scan (i.e. converted to values of percentage of maximum), and plotted vs. distance (µm) at each ~5 µm interval. Due to the difference in line scan lengths and the number of data points per unit length between samples, an averaging and aligning technique was used. Raman peak area vs. distance data for different samples were aligned with respect to the tessera–UC interface (i.e. setting the interface as the 0 µm point), binned in 10 µm increments. Each 10 µm bin was averaged, and standard deviations were calculated for the polyP and Pi peak areas.

3.3. Histology

Frozen, excised scapulocoracoid skeletal elements from a dogfish shark (*Squalus acanthias*) were sectioned to 20 µm with a cryo-microtome (Leica Biosystems CM1850) and mounted on glass microscope slides. ALP activity was identified with Sigma FAST™ BCIP/NBT (5-Bromo-4-chloro-3-indolyl phosphate/Nitro blue tetrazolium, Sigma-Aldrich) on fresh-cut sections. Optical images were acquired at 20× as described above.

TB (0.05%, Sigma-Aldrich), a non-specific stain for polyP, was applied to the sections for 5 min. The stained sections were lightly rinsed by pipetting deionized water directly onto the slide, and promptly imaged. As previously reviewed [7], the TB–polyP complex is metachromatic, turning a pink-purple color. Optical images at 20 \times were promptly acquired and later processed with ImageJ [52] (see below) to quantify how staining intensity changes in the UC with distance from the tessera–UC interface.

VK stains Pi by the production of silver phosphate [53]; as polyP forms a different complex with silver [6], a lack of VK staining is expected in polyP-rich areas (e.g. where the TB stain mentioned above turns pink-purple). VK stain (1% AgNO₃, Sigma-Aldrich) was applied by following the same procedure for TB, followed by exposure to sunlight for 5 min. VK-stained samples were lightly rinsed, and were not treated with sodium thiosulphate. Optical images were acquired and processed with ImageJ (see below).

3.4. Fluorescence microscopy

Frozen excised skeletal elements of *Urobatis halleri* were sectioned to \sim 100 μ m with a tissue slicer (Stoelting), and placed on glass microscope slides. 50 μ g ml⁻¹ of DAPI (Sigma-Aldrich), which forms a complex with polyP that is excitable with ultraviolet light, was applied to the section for \sim 2 min, and then lightly rinsed with deionized water. The region of interest (ROI) was identified promptly with light microscopy; the DAPI–polyP complex was then excited with a 405 nm laser. Emission spectra were acquired on a Nikon C1si confocal system equipped with a spectral detector, similar to methods previously described [7]. Fluorescent images were analyzed with Nikon NIS Elements AR and ImageJ software to measure the spectral signatures and total fluorescent intensity as a function of distance along a line drawn perpendicular through the tessera–UC interface, respectively.

The fluorescence maximum of the DAPI–polyP complex differs from the DAPI–DNA fluorescence maximum: when excited with UV light, the DAPI–DNA complex emission maximum occurs at 461 nm [54,55], whereas the DAPI–polyP emission maximum lies between 525 and 550 nm [39,40]. There is significant convolution of the DAPI–DNA and DAPI–polyP emission spectra in the regions between these maxima; however, to the right or left of this overlapping region, reasonable identification of each complex is possible. To distinguish these emissions, we considered fluorescent emissions in the range of 410–470 nm as indicators of DAPI–DNA association (i.e. fluorescence from the center-left of the DAPI–DNA spectrum, where little DAPI–polyP convolution is expected) and emissions in the range of 560–630 nm as indicators of DAPI–polyP fluorescence (i.e. to the right of the DAPI–polyP maximum, where minimal DAPI–DNA emission is expected), similar to previous analysis [7]. Even longer 670–730 nm wavelength images were collected and studied (data not shown). These images revealed signals distributed exclusively within the tesserae and UC at the mineralization front; these images were of lower brightness since they represent the tail end component of the DAPI–polyP emission curve. We gathered spectral data over three different ROIs: a wide ROI encompassing the tissues studied (i.e. including perichondrium, tesserae and UC up to \sim 500 μ m away) and smaller ROIs associated with specific tissues (a ROI containing tesserae and UC immediately adjacent, and a ROI of UC far from the mineralization front).

3.5. ImageJ processing

Histology and fluorescent microscopy images were analyzed with ImageJ [52] to measure the UC staining intensity and distance from the tessera–UC interface. One image was taken from each of

three to four independent sections. Following auto-brightness/contrast adjustment, the paintbrush tool (brush width 2) was used to trace the tessera–UC interface by hand, providing a distinct gray value of 255 (white) boundary to identify the tesserae–UC interface. A digital transect was created by drawing a 125 pixel (\sim 200 μ m) line on each image, perpendicular to and crossing the tessera–UC interface, similar to the line scan performed with Raman spectroscopy. Care was taken not to transect chondrocytes in the UC. The Plot Profile function was used to generate the gray value vs. distance output, indicating the staining intensity along the linear trace. The tessera–UC interface location was identifiable in the profile plot by its modified gray value (255 = white). This traced tessera–UC boundary was used to align different scans, allowing for statistical description of the gray value vs. distance between scans and between specimens. Three transects were generated for each image and average gray values at each distance point were calculated. The data from three or four independent sections were averaged and plotted. Error bars represent the standard deviation of intensity values between the independent sections.

This process of transect alignment and auto brightness–contrast modification allowed quantitative comparative analysis, among transects and images, of relative staining or fluorescence intensity differences vs. distance along transects perpendicular to the tessera–UC interface. No standard calibration for signal intensities could be performed because of variations in absolute intensity (e.g. between samples, measurement days, etc.); however, our analysis method allowed for the quantitative depiction of relative differences among samples and treatments (e.g. before and after ALP application).

3.6. ALP incubation

A bead of 10 U ml⁻¹ intestinal ALP (Sigma-Aldrich) was applied on 20 or 100 μ m sections of *Urobatis halleri* pectoral girdle, prepared at the same time as the histological samples mentioned above and mounted on glass microscope slides. These sections were placed on slides in a humidity-controlled incubator at 37 $^{\circ}$ C for 1 h. The sections were lightly washed, and stained with TB, DAPI or VK as described above to determine how staining patterns change following application of ALP.

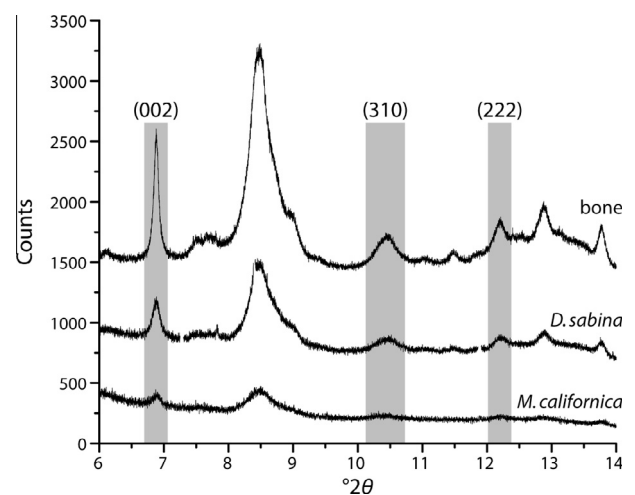


Fig. 3. Synchrotron powder diffraction patterns of emu tibial bone powder and tesserae from the pectoral girdle of the Atlantic stingray *Dasyatis sabina* and the bat ray *Myliobatis californica*. The diffraction peaks from apatite long (*c*-) axis (002) and transverse (222) and (310) axes were used to compare the crystallite sizes. The elasmobranch apatite crystals are smaller and/or less crystalline than bone apatite.

4. Results

4.1. Synchrotron powder diffraction

The diffraction patterns of mineralized tissue from the two stingray species (*D. sabina* and *M. californica*) are presented in Fig. 3. These results are overlaid with those of emu bone powder to confirm the apatite mineralogy, and compare the peak positions, size and shape. The peak positions are similar for all samples, yet the elasmobranch apatite diffraction peaks are less intense, and the FWHM values are larger. The crystallite size results are presented in Table 1.

4.2. Raman spectroscopy

A plot of the Pi peak area vs. distance shows a distinct transition from the Pi-containing tessera to the Pi-free UC (Fig. 4). An overlay of the polyP peak area vs. distance shows a roughly inverse correlation between Pi and polyP peak areas, with polyP increasing as Pi drops off at the tesseral margin.

4.3. ALP histology

BCIP–NBT staining identified ALP activity in the UC at the tessera–UC interface. ALP histology, as well as fluorescence microscopy and histology for polyP (see below), exhibited unexpected signals in cells in UC chondrocytes. Although our current methods do not allow adequate resolution for examination of these cellular features, we include our preliminary observations, as they are suggestive of cellular involvement in the mineralization process. ALP activity, for example, was located within the cells in the perichondrium, non-tesseral chondrocytes in the UC adjacent to the tesseral chondral edge, and in a halo of UC surrounding the ALP-positive chondrocytes (Fig. 5). However, chondrocytes in the UC further from the tessera–UC interface did not exhibit ALP activity. Given that tesseral cells (cells housed within tesserae [14]; Figs. 1 and 2) are surrounded by and can be obscured by mineral, especially in thicker sections, it was unclear in these preparations whether they stained positively for ALP activity.

4.4. Fluorescence microscopy and polyP/Pi histology

4.4.1. Fluorescence microscopy

DAPI-stained sections exhibited a general yellow-green fluorescence associated with perichondral cells, tesseral cells and chondrocytes within the UC (Fig. 6A). A yellow-green halo around UC chondrocytes was also observed, but was transient and faded rapidly. An intense yellow-green emission in the UC was observed in a swath ~60 μm wide adjacent to the tessera–UC interface (Fig. 6A). A line scan measuring fluorescence intensity as a function of UC distance perpendicular to this interface showed that this emission was most intense at the tesserae–UC interface and decreased with distance from the UC–tessera interface (Fig. 6C: black triangles).

Table 1

Apatite crystallite sizes calculated with the Scherrer equation.

Sample	Crystallite size (\AA)		
	(002)	(222)	(310)
Cortical bone (emu)	239.4	123.0	60.0
<i>D. sabina</i>	156.2	68.4	53.5
<i>M. californica</i>	147.4	77.9	50.0
Cortical bone (emu) [45]	209 \pm 2	–	62.9 \pm 0.6
Callous bone (human) [56]	200	190	80
Cortical bone (rat) [58]	168 \pm 4	–	56 \pm 1
Calcified cartilage (rat) [58]	122 \pm 18	–	46 \pm 2

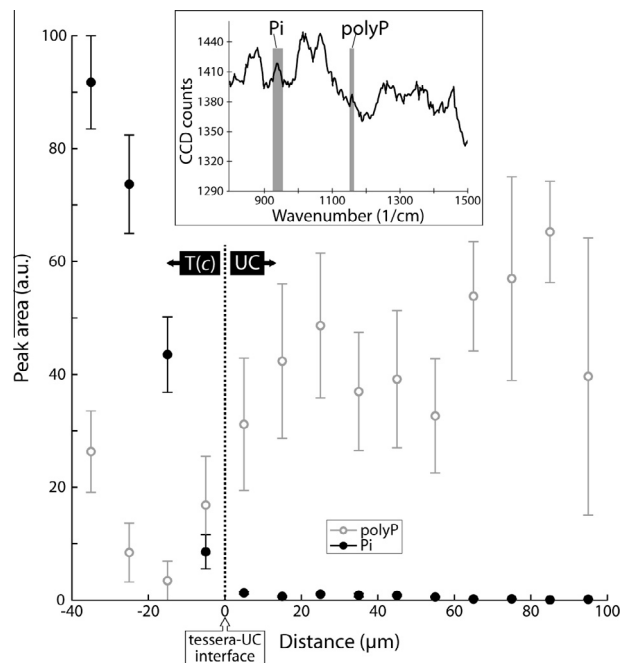


Fig. 4. Raman spectroscopic analysis of a cryo-sectioned jaw from the round stingray *Urobatis halleri*. Line scans of 100 μm in length were drawn across the tessera (T(c)–UC interface; see Fig. 2). To standardize across multiple line scans, transects were aligned so that the tesserae–UC interface was located at 0 μm distance on the x-axis; percentage maximum peak area values from four different samples were then averaged in 10 μm intervals, moving in the chondral direction (positive values) and tesseral direction (negative values). The normalized peak areas of the Raman spectra (example in inset) for polyP (1145–1175 cm^{-1}) and Pi (930–980 cm^{-1}) are plotted vs. distance along the line scan. PolyP and Pi peak area values are roughly negatively correlated.

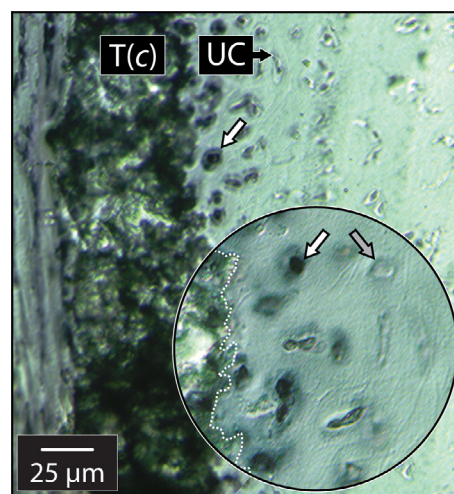


Fig. 5. BCIP–NBT staining for ALP of scapulocoracoid cross-sections at the tessera–UC interface from the spiny dogfish *Squalus acanthias*. Chondrocytes near the tessera (T(c)–UC interface (up to ~60 μm away) stained positively for ALP activity (white arrows), as did UC adjacent to the tesserae. A ring of UC surrounding the ALP-active cells also stained positively for ALP activity (magnified in the inset image; the white dashed line roughly marks the chondral edge of the tessera). Chondrocytes further in the UC (>60 μm away; gray arrow) did not stain positively for ALP activity.

After ALP treatment, the DAPI signal intensity from the UC region abutting the tesserae was reduced to a value similar to the UC at a distance from the tesserae (Fig. 6B and C, gray circles). Section 4.4.4 addresses the spectral analysis of the DAPI fluorescence emitted from these samples.

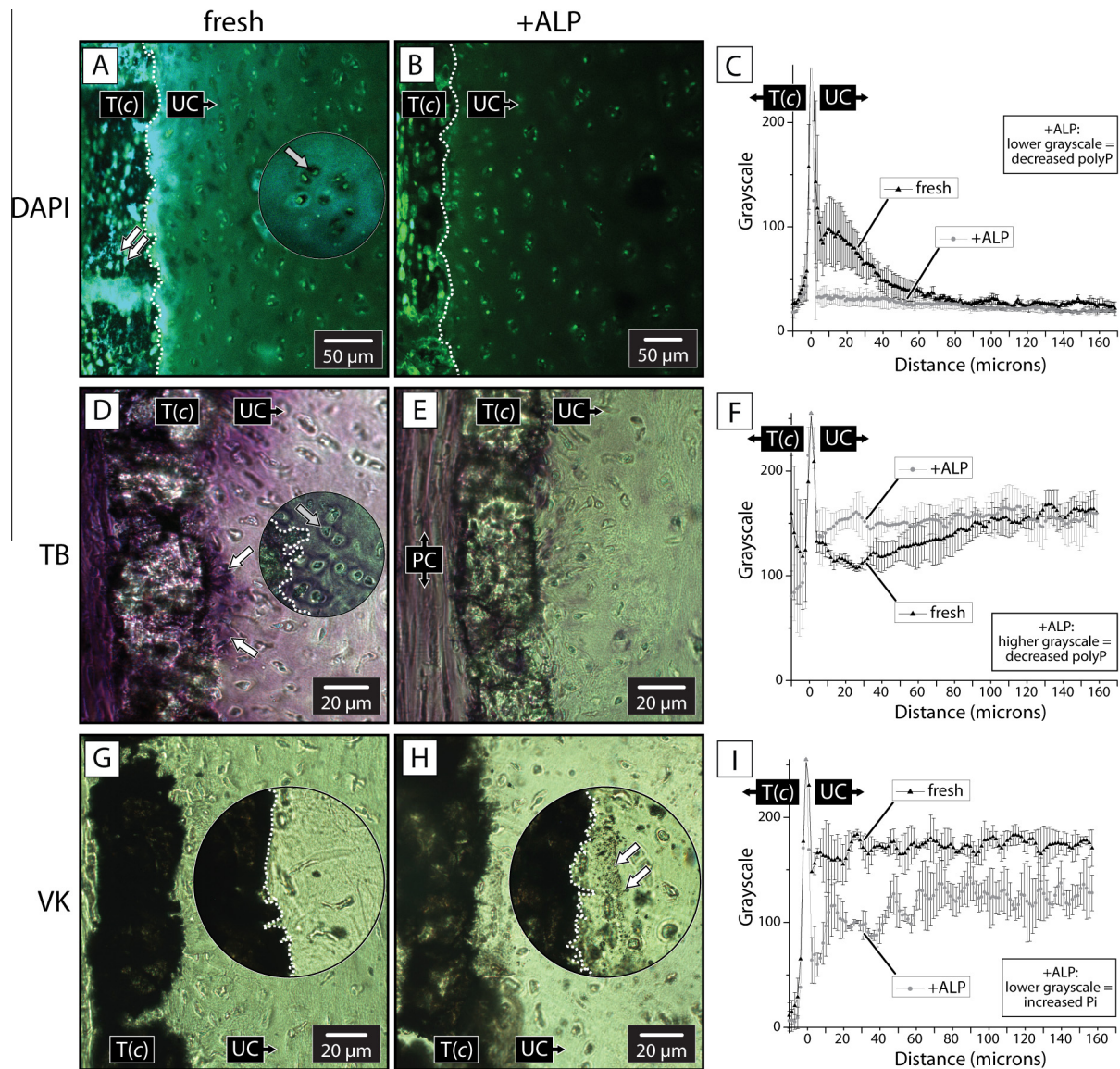


Fig. 6. Analysis of the tessera (T(c))–UC interface before (fresh; left column) and after application of exogenous ALP (+ALP; middle column). (A) Image of DAPI ($50 \mu\text{g ml}^{-1}$) fluorescence from fresh-cut tesserae and UC observed through a 525/25 nm filter, which detects both DAPI–polyP and DAPI–DNA emissions. Note white dashed line marking the tessera–UC interface. Bright DAPI emission was observed in the UC adjacent to the tesserae, within tesseral cells (white arrows) and chondrocytes (but apparently not in an unstained zone immediately around chondrocytes, indicated by the gray arrow in the inset image, taken from UC immediately adjacent to the chondral tesseral edge). (B) DAPI emissions reduced by ALP treatment. (C) ImageJ quantification of the gray values along a line drawn across and perpendicular to the tessera–UC interface. The lighter gray values near the tessera–UC interface for the freshly cut section (black triangles) are removed by ALP treatment (gray circles). (D) TB stains the UC adjacent to the tesserae (white arrows), and surrounding chondrocytes near the tesserae in the freshly cut section, supporting the DAPI-identified presence of polyP. The inset image shows a transient TB stain (gray arrow) that occurred outside chondrocytes immediately after application of stain but faded soon afterward (the white dashed line roughly marks the chondral edge of the adjacent tessera). (E) ALP treatment resulted in less TB staining. (F) Gray values along a line similar to (C). Lower (darker) gray values are observed in the UC close to the tesserae (dark triangles), which was not observed when the section was treated with ALP (gray circles). (G) VK staining of freshly cut sections. Pi in the mineralized tesserae stained a dark color while the UC remained unstained. (H) After ALP treatment, VK staining identified Pi in the UC adjacent to the tessera–UC interface (magnified inset, white arrows; compare with inset in (G); the white dashed line roughly marks the chondral edge of adjacent tesserae in both of these insets). (I) Gray value quantification of a line scan similar to (C) and (F). VK staining in the UC of the freshly cut section (dark triangles) was even and less dark than in ALP-treated sections. Gray values were lowest (darkest VK staining) in the ALP-treated UC next to the tesseral surface and increased (lighter VK staining) with distance from the tessera (lighter circles). The white boxes indicate the direction that grayscale data shift with addition of ALP, and how to interpret this shift in terms of presence of polyP or Pi.

4.4.2. PolyP histology with TB

TB stained tesseral chondrocytes, as well as chondrocytes adjacent to the tesseral chondral edge (Fig. 6D); the latter appear to be the same cells that stained positively for ALP, yet no co-staining was performed to verify this. TB also stained the UC immediately surrounding these chondrocytes, forming a purple halo around cells in this region (Fig. 6D). The UC region abutting the chondral tesseral edge stained a purple-pink color in cryo-cut, TB-stained samples (Fig. 6D); ImageJ analysis indicated that the highest matrix TB staining (i.e. lowest gray values) was localized in the

UC adjacent to the tessera–UC interface, with stain intensity decreasing with distance from tesserae (Fig. 6F, black triangles). After ALP treatment, this distinct purple UC staining at the tessera–UC border was not observed (Fig. 6E), as illustrated by the higher (lighter) and more uniform gray values in ImageJ analysis of UC staining (Fig. 6F, gray circles). The TB staining in the UC chondrocytes and cells in the perichondrium was also reduced after ALP treatment, although the fibers and extracellular matrix of the perichondrium retained TB staining. TB staining is not specific for polyP, so in situ ALP was applied to the section (see below) to

depolymerize polyP and see whether: (1) UC TB metachromatic staining would be removed; and (2) Pi, identified with VK staining, would appear in its place.

4.4.3. Pi histology with VK staining

In fresh-cut, VK-stained samples, tesserae stained positively for Pi, whereas the UC was largely unstained (Fig. 6G). The UC gray values were consistent throughout the UC tissue, with no difference between matrix abutting and further from the tessera–UC interface. After ALP treatment, VK staining indicated a darker UC region adjacent to the tessera–UC interface (Fig. 6H). VK staining was most intense within a distance of $\sim 60 \mu\text{m}$ of the tessera–UC interface (Fig. 6I), similar to the staining distribution distance observed with TB prior to ALP treatment (Fig. 6F). However, in the UC at a distance from the tessera–UC interface, there was also an increase in VK staining relative to fresh tissue. The perichondrium and some chondrocytes, both inside and outside of tesserae, also appeared to show some VK-positive staining after ALP treatment. Higher resolution methods are required to verify this observation.

4.4.4. Fluorescence spectral analysis

Fluorescence emissions obtained from the wide region of interest shown in Fig. 6A and B (including perichondrium, tesserae and both near- and far- field UC) were resolved with a spectral detector in fresh (Fig. 7A) and ALP-treated (Fig. 7B) samples. The spectral composition of the images were analyzed and plotted alongside the Nikon standard reference spectra for DAPI–DNA (Fig. 7C). Spectral analysis of the entire fresh-cut area exhibited a complex emission peak with left and right shoulders and a maximum of $\sim 525 \text{ nm}$, characteristic of the 525–550 nm DAPI–polyP complex emission [39,40] (Fig. 7C). It is possible that the 525–550 nm complex peak is the result of convoluted DAPI–DNA and DAPI–polyP emission. After ALP treatment, the peak position of the emission spectrum from the region in Fig. 7B was shifted to a position intermediate to DAPI–DNA and the fresh section fluorescence (Fig. 7C), and furthermore became narrower, suggesting a decrease in the DAPI–polyP component.

Bandwidth filtering to enhance the DAPI–DNA fluorescence component (410–470 nm) revealed tesseral cells, chondrocytes and perichondrial cells in fresh-cut samples (Fig. 8A). DAPI–polyP emission filtering (560–630 nm) showed fluorescence associated with cells in the UC, tesserae and perichondrium, and within the diffuse band of UC tissue adjacent to tesserae (Fig. 8B).

To compare the fluorescence spectral emissions from the UC at a distance from the tesserae with the emissions from the tesserae and their adjacent UC, spectral analysis was applied to two ROIs (see

Fig. 8A green vs. red ROI). Fluorescence from the UC distant from tesserae exhibited a spectrum with a peak maximum of 480 nm, an intermediate peak between DAPI–DNA and DAPI–polyP, suggesting a convolution between these emissions (Fig. 8C). The ROI containing only tesserae and the UC abutting the tesserae exhibited an emission maximum of 545 nm (Fig. 8C), suggesting that the DAPI–polyP emission component is greater in this region.

After ALP treatment, fresh tissue results were similar to spectral detector imaging for DAPI–DNA was similar to the fresh tissue results, with cell-associated fluorescence and low intensity fluorescence from the UC (Fig. 8D). Spectral detector imaging for DAPI–polyP showed continued cell-associated fluorescence in the UC and perichondrium, but fluorescence was absent from the band of UC adjacent to tesserae, and reduced or was absent in tesseral cells (Fig. 8E). At a distance from the tesserae, the fluorescence maximum was $\sim 480 \text{ nm}$, a peak wavelength similar to that from the equivalent ROI of the fresh section (Fig. 8C vs. F). In contrast, the ROI that included the tesserae and the UC abutting the tesserae exhibited an emission maximum of 480 nm with left and right shoulders (Fig. 8F), a greatly reduced emission maximum relative to the same ROI of a fresh section (Fig. 8C). This difference suggests that ALP treatment removed the higher wavelength DAPI–polyP emission component observed in the fresh section, which is concentrated in the UC at the tesserae–UC interface.

5. Discussion

Our data indicate co-occurrence of polyP and ALP in the UC immediately adjacent to the chondral surface of tesserae in elasmobranch tessellated cartilage, suggesting that this region is important in generating the mineralized material on the chondral surface of tesserae. Tesserae increase in both width and depth during ontogeny, with depth increases apparently accomplished in part by the chondral surface “advancing” over and engulfing chondrocytes in the UC beneath them [12,27]. The engulfed chondrocytes form a network of vital, interconnected tesseral cells, the function of which is unknown [12,14].

The motivation of this work was to examine the UC next to the mineralizing and expanding tesserae for possible apatite mineral precursors. Our identification and localization of ALP (Fig. 5) and polyP in adult tesserae (using a variety of different analytical techniques to identify and locate polyP; Figs. 4 and 6–8), suggests that ALP and polyP act in unison to generate biological apatite at the edges of growing tesserae. The detection of DAPI–polyP fluorescent emissions from chondrocytes, tesseral cells and perichondrial cells

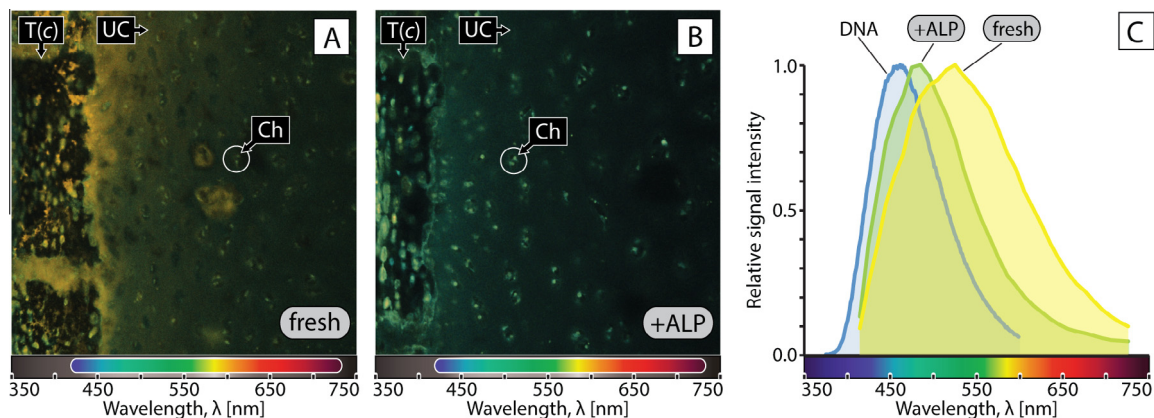


Fig. 7. Spectral detector images (410–730 nm) from DAPI-stained fresh-cut (A) and ALP-treated (B) skeletal sections, including tesserae and UC. A. The freshly cut section has an area near the UC that has a strong yellow–red component. (B) Spectral image of fluorescence from the ALP-treated section. (C) The emissions over the entire imaged areas in (A) (yellow) and (B) (green). The spectral scan data are compared with DAPI–DNA emission (blue). ALP treatment resulted in a narrower, leftward shifted overall emission.

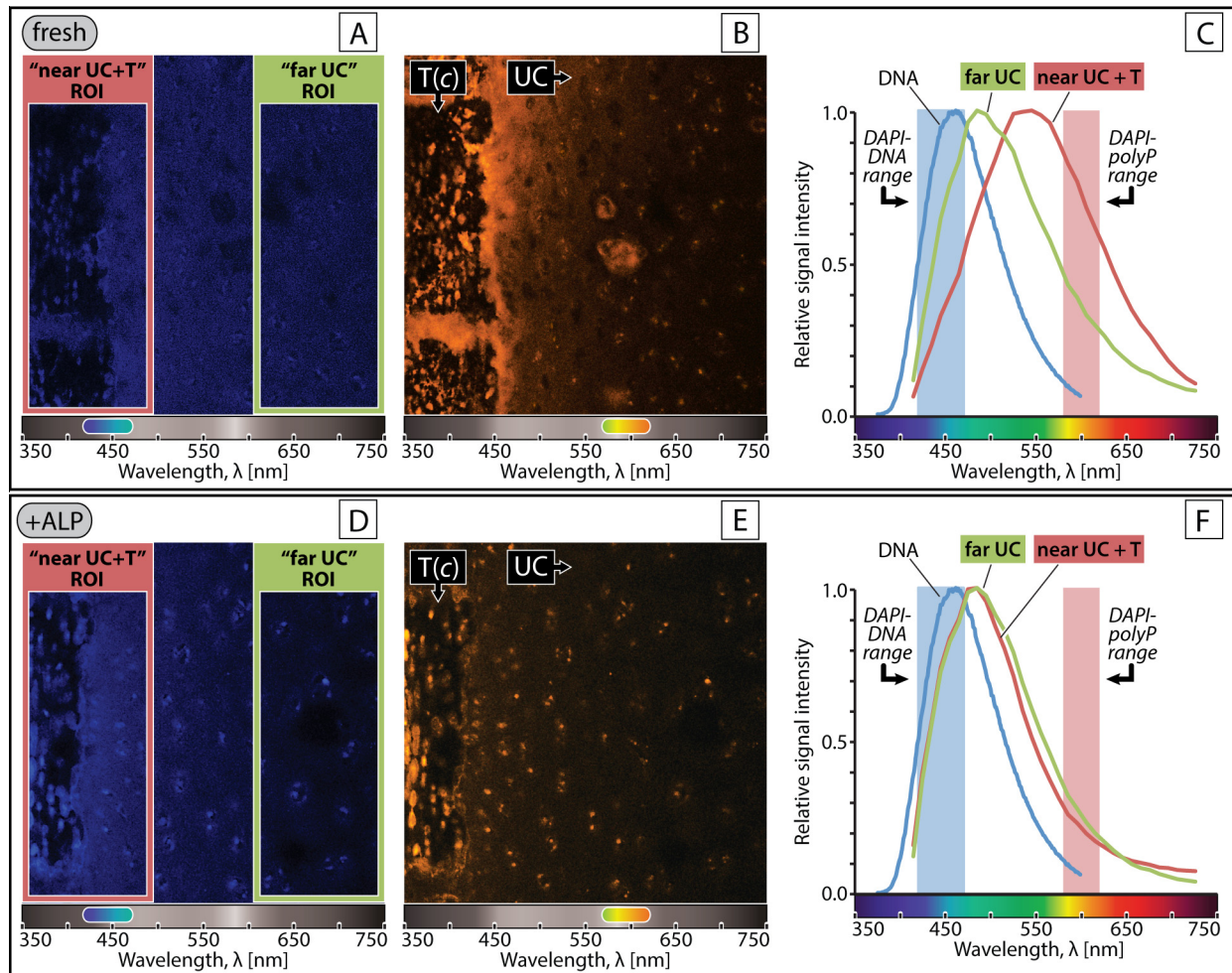


Fig. 8. (A) Image of emissions between 410 and 470 nm from a freshly cut section with two indicated ROIs: UC, green; tesserae with abutting UC, red. (B) Image showing emissions between 560 and 630 nm from the same freshly cut section shown in (A). (C) Spectral emissions from DAPI–DNA (blue), and emissions at regions defined by ROIs shown in (A) (tesserae, red; UC, green). (D) Image comprising spectral emissions between 410 and 470 nm from the ALP-treated section. (E) Image showing the 560–630 nm emissions from the same ALP-treated section shown in (D). (F) Plots of spectral emissions based on the ROIs appearing in (D): UC: green; tesserae with abutting UC: red.

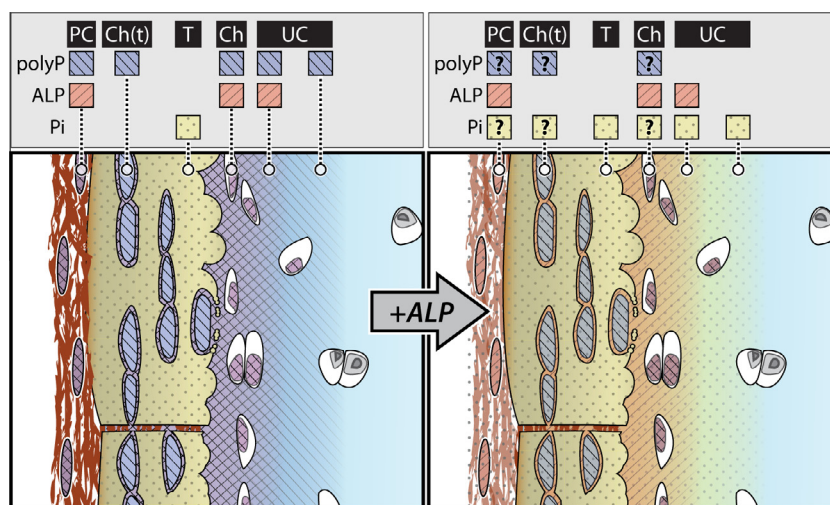


Fig. 9. Schematic summarizing the observed results of staining freshly cryo-cut (left-hand schematic) and ALP-treated (right-hand schematic) elasmobranch tessellated skeletal sections; compare with Fig. 2. Above each schematic, colored boxes indicate whether polyP, ALP and/or Pi occurred in the sample in a particular location; for example, polyP and ALP are indicated to co-occur in the perichondrium (PC) in fresh cryo-cut samples. PolyP and ALP also co-occurred in chondrocytes (Ch) near the tesserae, and the UC adjacent to the tesserae. The tesserae stained positively for Pi, and tesseral cells (Ch(t)) appeared to contain polyP. After ALP treatment, Pi was observed in the UC matrix adjacent to the tesserae, and in the perichondral cells, the tessera and tesseral cells. Pi was also seen in the chondrocytes near the tessera–UC interface. PolyP depolymerization by exogenous ALP treatment is proposed to have generated Pi. We observed evidence of polyP in tesseral and non-tesseral cells; however, this was an unexpected result and so our analysis of cellular components post-ALP treatment was cursory; these structures are annotated with question marks to indicate that they require further examination.

(summarized in Fig. 9) was unexpected and suggests that tesseral and non-tesseral chondrocytes may contain polyP. The indication that UC chondrocytes at the edges of expanding tesserae also exhibit ALP activity suggests that they may play an active role in dictating where ALP and polyP interact. This may help explain how tesseral cells are able to maintain a zone of unmineralized matrix around them despite being completely encompassed by mineralized tissue [12,27]. Our use of the 20× lens limited our ability to resolve and identify the exact intracellular location of polyP with respect to DNA (i.e. to see if both are localized to the nucleus and/or perinuclear cytoplasm); further investigation is warranted. Although chondrocytes associated with tesserae have not been seen to exhibit the hypertrophy and cell death characteristic of the mineralization process in mammalian calcified cartilage in endochondral bone [12,17], the fact that polyP and ALP are likely involved in both tessellated cartilage and mammalian bone and cartilage mineralization suggests some ancient parallels in the ways these very different tissues mineralize their extracellular matrix.

5.1. Synchrotron powder diffraction

To our knowledge, the only published XRD analyses of elasmobranch skeletal mineral were performed nearly half a century ago [42,43]. Our data support their results indicating the mineral in elasmobranch skeletons is apatite, the mineral in mammalian bone (Fig. 3). Powder XRD analysis of the apatite within emu cortical tibial bone was comparable with previous reported values for emu cortical bone [45], and synchrotron powder diffraction analysis of callous bone [56]. The smaller and broader XRD peaks of tesseral minerals, however, indicate that these apatitic minerals are smaller and/or more strained than bone apatite. This is similar to data reported for the skeleton of an acellular boned teleost fish [57], and also reflects the smaller crystallite sizes measured in calcified cartilage as compared to bone from the rat skeleton [58]. These differences between elasmobranch cartilage and bone crystallites may result from different tissue mineralization environments and/or biochemical processes, and may play a role in the different chemical and material properties between fish skeletal tissues and those of mammals [59,60].

5.2. PolyP identification

We used Raman spectroscopic analysis to identify polyP (via its PO_2^- symmetrical stretching vibration; Fig. 4) in the UC adjacent to the tessera–UC interface, as hypothesized (Figs. 2 and 9). TB staining and DAPI–polyP emission from freshly cut sections also suggest that polyP is in the UC at the tessera–UC interface (Figs. 6A–F, 7 and 8). The TB and DAPI techniques also indicated a halo of polyP in the UC, outside of polyP-containing chondrocytes (Fig. 6A and D). We observed a small unstained region between the chondrocyte and its halo that appeared to be free of both ALP and polyP in our preparations (Fig. 6D); this is supported by Clement [27], who noted that, at the mineral front, the pericellular zone immediately around elasmobranch chondrocytes initially remains free of the advancing “pioneer mineralization” and only later do the lacunae walls encroach into the pericellular space. PolyP was also identified by DAPI fluorescence associated with tesseral cells, perichondral cells and chondrocytes in the UC (Figs. 6A–C, 7 and 8). This finding suggests an interesting relationship between polyP, chondrocytes, their pericellular spaces and the mineralization process; a deeper understanding requires additional study with higher resolution.

To initiate mineralization, the secretory theory postulates that cells responsible for mineralization secrete precursors and initiators into the extracellular matrix. We propose that polyP could be a metastable, Pi-providing mineralization component, and ALP

could be the mineralization initiator. Eames et al. [5] described localized ALP expression in non-mineralized, embryonic swell-shark (*Cephaloscyllium ventriosum*) cartilage, likely presaging the location of the first tesserae. Our data are the first demonstration of localized ALP activity in the adult tessellated skeleton, colocalizing ALP with elasmobranch skeletal mineralization. The proposal that polyP is an ALP substrate and a bioavailable Pi source for apatite biomineralization requires further development of identification and sample preparation methods, and investigation into the origin of polyP in mineralizing tissues.

The cellular production of polyP has been identified in eukaryotic mitochondria [61] – which are common to chondrocytes [63,64] and osteoblasts [65] – and a role for mitochondria in mineralization was previously proposed [62]. As preliminary evidence suggests that polyP may be involved in both tessellated cartilage and bone mineralization, the ability of mitochondria to concentrate and store Pi as polyP may have been an asset for bony and cartilaginous skeletal cells to biochemically control the production of extracellular apatite deposits.

The mechanisms involved in regulation of mineralization of the tessellated skeleton are largely unexamined, but there are suggestions of mineral precursors active in other elasmobranch mineralized tissues. During examination of elasmobranch dentin-forming cells, Sasagawa [66] identified “dark cells” that were associated with dentin mineralization. Their cytoplasm included “a well-developed Golgi apparatus, many mitochondria, electron-dense granules, and vesicles”. These components were also identified in the cells associated with enameloid mineralization [66]. It was postulated that the electron-dense granules might be mineral precursors, but their composition was not defined. The use of the Golgi apparatus to transport mitochondrial components is not characterized, but pre-Golgi secretory proteins have been identified in a mitochondria-associated membrane fraction [67]; we therefore postulate a possible connection to a secretory pathway.

Mitochondrial production of concentrated, amorphous, bioavailable P-stores as polyP presents a theoretically elegant strategy for biochemical accumulation of P, which could be secreted via the Golgi to the extracellular matrix to await depolymerization to Pi by ALP. Boonrungsiman et al. [68] recently captured an image of interaction between a mitochondrion and a P-rich vesicle with high angle-annular dark-field scanning transmission electron microscope, when samples of mineralizing cultured osteoblast cells were processed with high-pressure freezing and freeze-substitution. They attributed this to the formation of a Pi precursor for bone mineralization. However, as energy-dispersive X-ray spectroscopy identifies P, not Pi, the speciation of P cannot be positively identified. It is possible that the P-rich vesicle contained polyP rather than Pi, as the low-temperature methodology of Boonrungsiman et al. would allow adequate stabilization of polyPs, which are otherwise only transiently visible in other sample preparations.

5.3. ALP identification

BCIP–NBT staining identified ALP activity at the tessera–UC interface, confirming the original hypothesis (Figs. 2 and 9). ALP activity was also observed within chondrocytes adjacent to the chondral tesseral margin, and cells within the perichondrium (Figs. 5 and 9), whereas ALP activity could not be clearly detected in tesseral cells. ALP activity was also identified in the UC immediately surrounding the ALP-positive chondrocytes, in the same UC region where polyP was also observed.

5.4. Ex vivo ALP-treatment

In vitro, acid-catalyzed polyP depolymerization to Pi in aqueous solutions was previously measured with Raman spectroscopy [37].

Rather than employing acidic conditions, we tested the uncontrolled depolymerization of polyP to Pi within elasmobranch skeletal tissue by incubating fresh-cut samples with exogenous ALP (Figs. 6–8). After ALP incubation, polyP content decreased and Pi was detected in areas that had been rich in polyP in fresh samples: in the UC and chondrocytes abutting the tesserae and the cells of the tesserae (Fig. 9). However, cellular compartments in the UC and perichondrium that fluoresced with an emission maximum intermediate to DAPI–DNA and DAPI–polyP were less affected by exogenous ALP application, perhaps due to their protection from exposure and/or reduced reactivity to exogenous ALP (Fig. 8).

6. Conclusions

A tiled cartilaginous skeleton is a defining phylogenetic characteristic of the shark and ray clade, yet the chemical mechanisms for apatite mineralization at the tessera margins had not been explained. We suggest that, at the tesseral chondral mineralization front, apatite may form following a local release of Pi due to polyP depolymerization by ALP in the extracellular matrix. This may be a fundamental mechanism of tesseral growth, at least in the chondral direction. Exposing cryo-microtomed sections to exogenous ALP treatment decreased polyP content at the tesserae–UC interface and Pi was identified in its place. This *ex vivo*, *in situ* demonstration of Pi formation by polyP depolymerization with ALP supports the hypothesis that polyPs are a Pi source for apatite biomineralization in elasmobranch calcifying cartilage. This supports Robison's hypothesis [4] that an enzymatically controlled Pi-concentration increase within mineralizing tissue could be achieved by cleaving “an organic ester of phosphoric acid”.

The observation of polyP in all cell types examined in this study, its resistance to depolymerization by exogenous ALP application and its colocalization with ALP in chondrocytes in and around tesserae were unexpected. Focused higher-resolution examinations of elasmobranch chondrocytes and their surrounding microenvironments will surely provide insight into the regulation of mineralization in this system and possible cellular role(s) for polyP within elasmobranch skeletal cells. Overall, the observed parallels between mineralizing tessellated cartilage and other apatitic mineralizing tissues suggest that the association of ALP and polyP may be a shared and ancient enzymatic apatite biomineralization control strategy for a wide variety of organisms.

Acknowledgements

The authors thank Dr Adam Summers (Friday Harbour Laboratories, University of Washington) for the *Squalus acanthias* skeletal elements; Kady Lyons and Chris Lowe for *Urobatis halleri* specimens; and Pepijn Kamminga and Kerin Claeson for the computed tomography (CT) scan data in Fig. 1. The Beamline 11-BM data were kindly provided by the Advanced Photon Source at Argonne National Laboratory. This diffraction work was supported by the U.S. Department of Energy, Office of Science, Office of Basic Energy Sciences, under Contract No. DE-AC02-06CH11357. Drs. Matt Harrington, Admir Masic, Roman Schuetz and Clemens Schmitt are thanked for sharing their Raman expertise. Philip Pelletier is thanked for providing support and access to the CAREG facility for cryo-sectioning. Stephanie McMillan is thanked for her help imaging histological slides, and the imaging resources of Professor Akimenko's laboratory are also acknowledged. Dr Marianne Ariganello is thanked for her helpful assistance with histology. S.O. acknowledges the DAAD for providing research support through their Research Visit Grant for Faculty, and use of the Raman spectrometer in the Department of Biomaterials at the Max Planck Institute of Colloids and Interfaces (Postdam-Golm).

Dr Stuart Stock (Northwestern University Feinberg School of Medicine) is thanked for assistance with the powder diffraction analysis. We thank Dr. Kevin Conway and Charles Magalhaes of Nikon Canada for their imaging-analysis help. The Natural Sciences and Engineering Research Council of Canada is thanked for the Discovery Grant that supports S.O., and supported the majority of this work. M.N.D. is supported by a Human Frontier Science Program Young Investigator Fellowship (RGY0067) and Gottfried Wilhelm Leibniz-Preis 2010 (DFG - FR 2190/4-1). The helpful and thorough feedback from the reviewers is appreciated and greatly improved the manuscript.

Appendix A. Figures with essential color discrimination

Certain figures in this article, particularly Figs. 1, 2, and 5–9, are difficult to interpret in black and white. The full color images can be found in the on-line version, at <http://dx.doi.org/10.1016/j.actbio.2014.06.008>.

References

- [1] Currey JD. The design of mineralised hard tissues for their mechanical functions. *J Exp Biol* 1999;202:3285–94.
- [2] Currey JD. *Bones: structure and mechanics*. Princeton, NJ: Princeton University Press; 2002.
- [3] Lowenstam HA, Weiner S. *On biomineralization*. Oxford: Oxford University Press; 1989.
- [4] Robison R. The possible significance of hexosephosphoric esters in ossification. *Biochem J* 1923;17:286.
- [5] Eames BF, Allen N, Young J, Kaplan A, Helms JA, Schneider RA. Skeletogenesis in the swell shark *Cephaloscyllium ventriosum*. *J Anat* 2007;210:542–54.
- [6] Van Wazer JR, Campanella DA. Structure and properties of the condensed phosphates. IV. Complex ion formation in polyphosphate solutions. *J Am Chem Soc* 1950;72:655–63.
- [7] Omelon S, Georgiou J, Henneman ZJ, Wise LM, Sukhu B, Hunt T, et al. Control of vertebrate skeletal mineralization by polyphosphates. *PLoS One* 2009;4:e5634.
- [8] Kornberg A. Inorganic polyphosphate: toward making a forgotten polymer unforgettable. *J Bacteriol* 1995;177:491–6.
- [9] Mahamid J, Sharir S, Gur D, Zelzer E, Addadi L, Weiner S. Bone mineralization proceeds through intracellular calcium phosphate loaded vesicles: a cryo-electron microscopy study. *J Struct Biol* 2011;174:527–35.
- [10] Landis WJ, Hauschka BT, Rogerson CA, Glimcher MJ. Electron microscopic observations of bone tissue prepared by ultracytometry. *J Ultrastruct Res* 1977;59:185–206.
- [11] Landis WJ, Glimcher MJ. Electron diffraction and electron probe microanalysis of the mineral phase of bone tissue prepared by anhydrous techniques. *J Ultrastruct Res* 1978;63:188–223.
- [12] Dean MN, Mull CG, Gorb SN, Summers AP. Ontogeny of the tessellated skeleton: insight from the skeletal growth of the round stingray *Urobatis halleri*. *J Anat* 2009;215:227–39.
- [13] Dean MN, Summers AP. Mineralized cartilage in the skeleton of chondrichthyan fishes. *Zoology* 2006;109:164–8.
- [14] Dean M, Socha J, Hall B, Summers A. Canalliculi in the tessellated skeleton of cartilaginous fishes. *J Appl Ichthyol* 2010;26:263–7.
- [15] Ashhurst DE. The cartilaginous skeleton of an elasmobranch fish does not heal. *Matrix Biol* 2004;23:15–22.
- [16] Huber DR, Neveu DE, Stinson CM, Anderson PA, Berzins IK. Mechanical properties of sand tiger shark (*Carcharias taurus*) vertebrae in relation to spinal deformity. *J Exp Biol* 2013;216:4256–63.
- [17] Kemp NE, Westrin SK. Ultrastructure of calcified cartilage in the endoskeletal tesserae of sharks. *J Morphol* 1979;160:75–101.
- [18] Egerbacher M, Helmreich M, Mayrhofer E, Böck P. Mineralisation of the hyaline cartilage in the small-spotted dogfish *Scyliorhinus canicula* L. *Scripta Medica (BRNO)* 2006;79:199–212.
- [19] Dean MN, Chiou W-A, Summers AP. Morphology and ultrastructure of prismatic calcified cartilage. *Microsc Microanal* 2005;11:1196–7.
- [20] Thompson DW. *On Growth and Form*. Mineola, NY: Dover Publications Inc; 1942. 1116 pp.
- [21] Maximow A. Untersuchungen über Blut und Bindegewebe. *Arch Mikros Anat* 1910;76:1–113.
- [22] Kashiwa HK, Komorous J. Mineralized spherules in the cells and matrix of calcifying cartilage from developing bone. *Anat Rec* 1971;170:119–27.
- [23] Ali S, Sajdera S, Anderson H. Isolation and characterization of calcifying matrix vesicles from epiphyseal cartilage. *Proc Natl Acad Sci* 1970;67:1513–20.
- [24] Lester KS, Ash MM. Scanning electron microscopy of mineralized cartilage in rat mandibular condyle. *J Ultrastruct Res* 1980;72:141–50.
- [25] Watt JC. The development of bone (A) the process of development of bones of different types; (B) normal physiologic calcification of the matrix in cartilage

- and in bone; (C) the problem of the manner of deposition of the calcium salts. Arch Surg 1928;17:1017–46.
- [26] Pautard F. Calcium phosphate microspheres in biology. Prog Cryst Growth Charact 1981;4:89–98.
- [27] Clement J. Re-examination of the fine structure of endoskeletal mineralization in chondrichthyans: implications for growth, ageing and calcium homeostasis. Mar Freshw Res 1992;43:157–81.
- [28] Bonucci E. Fine structure and histochemistry of “calcifying globules” in epiphyseal cartilage. Z Zellforsch Mikrosk Anat 1970;103:192–217.
- [29] Christoffersen J, Christoffersen MR, Kibalczyk W, Andersen FA. A contribution to the understanding of the formation of calcium phosphates. J Cryst Growth 1989;94:767–77.
- [30] VanWazer JR. Phosphorus and its compounds. Vol. 1: chemistry. New York: Interscience; 1958.
- [31] Omelon S, Baer A, Coyle T, Pilliar RM, Kandel R, Grynblas M. Polymeric crystallization and condensation of calcium polyphosphate glass. Mater Res Bull 2008;43:68–80.
- [32] Millán JL. Mammalian alkaline phosphatases. New York: Wiley; 2006.
- [33] Kashiwa HK. Mineralized spherules in cartilage of bone revealed by cytochemical methods. Am J Anat 1970;129:459–65.
- [34] Marchesini N, Ruiz FA, Vieira M, Docampo R. Acidocalcisomes are functionally linked to the contractile vacuole of *Dictyostelium discoideum*. J Biol Chem 2002;277:8146–53.
- [35] Hirschman A. Staining of fresh epiphyseal cartilage with toluidine blue. Histochemie 1967;10:369–75.
- [36] Landis WJ, Glimcher MJ. Electron optical and analytical observations of rat growth plate cartilage prepared by ultracryomicrotomy: the failure to detect a mineral phase in matrix vesicles and the identification of heterodispersed particles as the initial solid phase of calcium phosphate deposited in the extracellular matrix. J Ultrastruct Res 1982;78:227–68.
- [37] De Jager H-J, Heyns AM. Study of the hydrolysis of sodium polyphosphate in water using Raman spectroscopy. Appl Spectrosc 1998;52:808–14.
- [38] Majed N, Matthäus C, Diem M, Gu AZ. Evaluation of intracellular polyphosphate dynamics in enhanced biological phosphorus removal process using Raman microscopy. Environ Sci Technol 2009;43:5436–42.
- [39] Allan R, Miller J. Influence of S-adenosylmethionine on DAPI-induced fluorescence of polyphosphate in the yeast vacuole. Can J Microbiol 1980;26:912–20.
- [40] Gomes FM, Ramos IB, Wendt C, Girard-Dias W, De Souza W, Machado EA, et al. New insights into the in situ microscopic visualization and quantification of inorganic polyphosphate stores by 4',6'-diamidino-2-phenylindole (DAPI)-staining. Eur J Histochem 2013;57:e34.
- [41] Siderius M, Musgrave A, van den Ende H, Koerten H, Cambier P, van der Meer P. *Chlamydomonas eugametos* (chlorophyta) stores phosphate in polyphosphate bodies together with calcium. J Phycol 1996;32:402–9.
- [42] Applegate SP. A survey of shark hard parts. In: Gilbert PW, Mathewson RF, Rall DP, editors. Sharks, Skates and Rays. Maryland: Johns Hopkins Press; 1967. p. 37–66.
- [43] Urist MR. Calcium and phosphorus in the blood and skeleton of the Elasmobranchii. Endocrinology 1961;69:778–801.
- [44] Wynnkyj C, Omelon S, Willett T, Kyle K, Goldberg H, Grynblas M. Mechanism of bone collagen degradation due to KOH treatment. BBA-Gen Subjects 2011;1810:192–201.
- [45] Wynnkyj C, Omelon S, Savage K, Damani M, Chachra D, Grynblas MD. A new tool to assess the mechanical properties of bone due to collagen degradation. Bone 2009;44:840–8.
- [46] Burr DB. The contribution of the organic matrix to bone's material properties. Bone 2002;31:8–11.
- [47] Wynnkyj C, Willett TL, Omelon S, Wang J, Wang Z, Grynblas MD. Changes in bone fatigue resistance due to collagen degradation. J Orthop Res 2011;29:197–203.
- [48] Wang J, Toby BH, Lee PL, Ribaud L, Antao SM, Kurtz C, et al. A dedicated powder diffraction beamline at the advanced photon source: commissioning and early operational results. Rev Sci Instrum 2008;79.
- [49] Toby BH. CMPR – a powder diffraction toolkit. J Appl Crystallogr 2005;38:1040–1.
- [50] Wopenka B, Pasteris JD. A mineralogical perspective on the apatite in bone. Mater Sci Eng C Mater Biol Appl 2005;25:131–43.
- [51] Ray NH. Oxide glasses of very low softening point: III, Study of potassium lead phosphate glasses by Raman spectroscopy. Glass Technol 1975;16:107–8.
- [52] Abramoff MD, Magalhães PJ, Ram SJ. Image processing with ImageJ. Biophotonics Int 2004;11:36–42.
- [53] Meloan SN, Puchtler H. Chemical mechanisms of staining methods: von Kossa's technique: what von Kossa really wrote and a modified reaction for selective demonstration of inorganic phosphates. J Histotechnol 1985;8:11–3.
- [54] Russell W, Newman C, Williamson D. A simple cytochemical technique for demonstration of DNA in cells infected with mycoplasmas and viruses. Nature 1975;253:461–2.
- [55] Williamson D, Fennell D. The use of fluorescent DNA-binding agent for detecting and separating yeast mitochondrial DNA. Methods Cell Biol 1976;12:335–51.
- [56] Peters F, Schwarz K, Epple M. The structure of bone studied with synchrotron X-ray diffraction, X-ray absorption spectroscopy and thermal analysis. Thermochim Acta 2000;361:131–8.
- [57] Moss ML, Posner AS. X-ray diffraction study of acellular teleost bone. Nature 1960;188:1037–8.
- [58] Arsenault AL, Grynblas MD. Crystals in calcified epiphyseal cartilage and cortical bone of the rat. Calcif Tissue Int 1988;43:219–25.
- [59] Liu X, Dean MN, Youssefpour H, Summers AP, Earthman JC. Stress relaxation behavior of tessellated cartilage from the jaws of blue sharks. J Mech Behav Biomed Mater 2014;29:68–80.
- [60] Cohen L, Dean MN, Shipov A, Atkins A, Monsonego-Ornan E, Shahar R. Comparison of structural, architectural and mechanical aspects of cellular and acellular bone in two teleost fish. J Exp Biol 2012;215:1983–93.
- [61] Macfarlane MG. Phosphorylation in living yeast. Biochem J 1936;30:1369.
- [62] Shapiro IM, Greenspan JS. Are mitochondria directly involved in biological mineralisation? Calcif Tissue Int 1969;3:100–2.
- [63] Sutfin LV, Holtrop ME, Ogilvie RE. Microanalysis of individual mitochondrial granules with diameters less than 1000 angstroms. Science 1971;174:947–9.
- [64] Martin J, Matthews J. Mitochondrial granules in chondrocytes. Calcif Tissue Res 1969;3:184–93.
- [65] Landis WJ, Paine MC, Glimcher MJ. Use of acrolein vapors for the anhydrous preparation of bone tissue for electron microscopy. J Ultrastruct Res 1980;70:171–80.
- [66] Sasagawa I. Mineralization patterns in elasmobranch fish. Microsc Res Tech 2002;59:396–407.
- [67] Rusiñol AE, Cui Z, Chen MH, Vance JE. A unique mitochondria-associated membrane fraction from rat liver has a high capacity for lipid synthesis and contains pre-Golgi secretory proteins including nascent lipoproteins. J Biol Chem 1994;269:27494–502.
- [68] Boonrungsiman S, Gentleman E, Carzaniga R, Evans ND, McComb DW, Porter AE, et al. The role of intracellular calcium phosphate in osteoblast-mediated bone apatite formation. Proc Natl Acad Sci USA 2012;109:14170–5.